



A comparative study of interface characteristics and properties of bronze coatings on steel by plasma arc and cold metal transition deposition

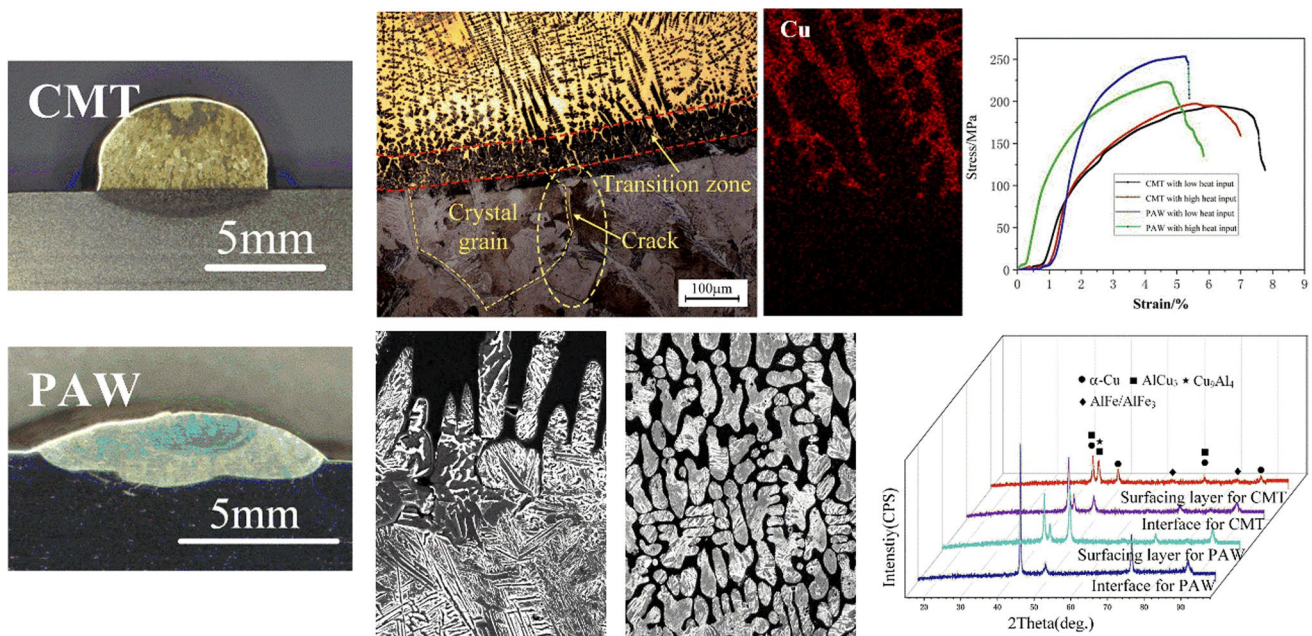
Yanming Wu^{1,3} · Xinghua Wang¹ · Jintian Zhang¹ · Zhi Li¹ · Chenghui Hu¹ · Wei Meng⁴ · Jiguo Shan^{2,3}

Received: 7 July 2023 / Accepted: 12 November 2023 / Published online: 29 January 2024
© The Author(s), under exclusive licence to Springer-Verlag GmbH, DE part of Springer Nature 2023

Abstract

A comparative study of bronze coatings on steel produced by plasma and cold metal transfer wire-arc depositing was carried out. The microstructure, interface characteristics, hardness, and shear bond strength of bronze deposits were investigated. Cold metal transition (CMT) deposition presented lesser penetration cracks and lower dilution than that of plasma arc deposition (PAD). The interfacial bonding of CMT deposits appeared as diffusion bonding characteristics, whereas PAD achieved a good metallurgical bond. Plasma arc deposited specimens showed more severe penetrating cracks and less CMT due to the difference of dilution rate. As heat input increased, microstructure of CMT and PAD deposited layer transformed from α -Cu + spherical or dendritic Fe-rich phase to massive Fe-rich phase + ϵ -Cu. The volume percentage of α -Cu + γ_1 in CMT deposits was observed higher than that of PAD, and Fe-rich phase in the PAD was significantly higher than that of CMT, leading in a significant increase of microhardness of PAD. Interfacial bonding strength of PAD under high heat input was much higher than that of CMT.

Graphical abstract



Keywords Aluminum bronze · Plasma arc deposition · Interface characteristics · Penetrating crack

Extended author information available on the last page of the article

1 Introduction

Aluminum bronze alloys exhibit relatively perfect corrosion resistance in sea water, favorable antifriction properties, thermal and electrical conductivity, and resistance to fouling by micro-organisms in sea water, hence providing the required set of properties for the ocean engineering [1, 2]. It is reasonable to replace cast bronze parts with bimetal ones to conserve insufficient nonferrous metals and boost fabrication strength. Objects composed of steel/bronze bimetal constructions are increasingly being used in numerous industries. One of the effective methods of manufacturing bimetal structures can be wire-arc surfacing [3, 4]. Thus, the development of material and technology for surfacing and depositing of bronze on steel has a bright future.

Cladding (welding) of copper on steels (with steels) has characteristics that have been noticed in domestic and international research [5–7]. As a result of copper alloys depositing on steel in the melting area, the two metals from a material differ significantly in terms of composition, microstructure, and base metal properties. Cladding modifies the surface of metallic materials to achieve the appropriate service qualities. Significant metallurgical and technological difficulties are encountered when depositing copper alloys on steel, including an increased tendency to pores formation (both in the deposited metal and along the fusion line with steel), intercrystalline penetrations of bronze into steel, and the possibility of alloying the deposited metal with iron, a high content of which deteriorates operational properties of the deposited bronze [8, 9]. As a result, the dilution rate has a significant impact on the creation of penetrating cracks and mechanical properties throughout the deposition process.

A wide range of depositing processes have been reported for copper alloys surfacing on steel which includes Shielded Metal Arc welding (SMAW) [10], Gas Tungsten Arc welding (GTAW) [11], Gas Metal Arc welding (GMAW) [12], laser cladding [13], and thermal spray [14]. The high-energy intensity of laser depositing process results in an overwhelmingly low level of dilution as compared to all the above-mentioned conventional welding processes along with a finer dendritic structure [14]. Cold metal transfer (CMT) welding and plasma arc welding (PAW) are new types of non-melting pole and melting arc welding method with low heat input. CMT has revolutionized the welding of dissimilar metals and lightweight alloy and improved bead formation, with controlled heat input and metal droplet transfer, which relies on filler wire

(electrode) short circuit and precise wire control for material transfer [15]. CMT process has been suggested for cladding and repair of Inconel 718 in turbine application [16]. Solecka et al. [17] deposited Inconel 625 over carbon steel by CMT. PAW is a high-energy beam non-molten arc welding with concentrated arc energy, small weld deformation, and stable welding process. Levin et al. [18] deposited Inconel 625 and SS 316L weld overlays over carbon steel using PAW. Plasma arc welding process with powder deposition has been reported to be of controlled dilution levels (5–30%) for a high deposition rate [19]. Recently, the hardfacing of copper alloys on steel using CMT was reported, and the dilution levels in the monolayer coating are exceedingly low (3–4%) and comparable to plasma arc deposition (PAD) and laser depositing due to low heat input [20]. CMT and PAD are attractive choices for surface deposition and large component fabrication due to their exceptional advantages. Furthermore, the weld formation differs greatly between CMT and PAD due to dilution rate differences, and the characteristics of deposits created in bronze alloys using the aforesaid procedure are currently limited [11, 21–23]. As a result, further research into the correlation mechanism between dilution rate and interfacial behavior is required to improve the microstructure and characteristics of copper/steel bimetals.

In this work, a comparison of aluminum-bronze cladding on steel using CMT and PAD methods was reported. The effect of dilution rate on the chemical distribution, microstructure, and shear strength of aluminum-bronze depositing on steel of both CMT and PAD process were investigated. The interface behavior of aluminum-bronze deposited layers prepared by the two processes was analyzed. The aim of the work described in this paper was the determination of forming adaptability, microstructure, and bonding strength of bronze wire-arc depositing on steel for CMT and PAD.

2 Experimental procedure

The mild steel substrate was produced from Magang (Group) Holding Co., Ltd. (China) (130 mm × 75 mm × 30 mm). The Cu alloy wire was supplied by Tianjin Bridge Welding Materials Group Co., Ltd. (China) with a diameter of 1.2 mm. The chemical compositions of base metal and welding wire are listed in Table 1. The surface of the base steel was cleaned with an electric sander prior to wire-arc deposition to eliminate oil and rust.

A Fronius TPS 5000 CMT welder and a VR7000 wire feeder from Austria were used for wire-arc deposition.

Table 1 Compositions of mild steel and copper alloy wire (wt%)

Element	C	Si	Mn	Al	Fe	Cu
S214				7.5	0.5	Bal
Mild steel	0.2	0.5	1.7		Bal	

Welding torch was manipulated by external means using a self-developed computer numerical control (CNC) machine. Plasma arc deposition on mild steel surfaces was performed using a Fronius Trans Tig 5000 Job G/F power supply and a Plasma Module 10 plasma generator. The wire feeder was a self-developed side-axis wire feeder with the model SB-10-500. Plasma arc welding head was attached to a 6-axis KUKA robot linked to a 2-axis table. The process was carried out using plasma arc welding torch in the argon atmosphere. Pure argon gas was used as shielding gas in CMT and plasma arc depositing. The depositing parameters of CMT and PAD are given in Table 2.

Figure 1 shows optical images of weld geometry of CMT and PAD deposited specimen. Based on the morphological characteristics of deposition layer, the dilution rate η and the wetting angle α are measured. As depicted in Fig. 1, the geometrical dimensions (H_D —height, W_D —width, D_F —depth of fusion, and α —contact angle) of deposited layers were measured on the cross-sections of representative samples. Dilution levels of the deposited samples were determined by dividing the fusion zone into two areas including the melted copper (A_1) and the melted area of base steel (A_2).

Table 2 Process parameters used for CMT and PAD deposition

Process parameters	Values	
	CMT	PAD
Wire feed speed/m/min	2.6–5.6	3–6
Current/A	80–160	60–140
Voltage/V	17–21	16–19
Protection gas (Ar) flow rate/L/min	25	25
Plasma gas (Ar) flow rate/L/min	–	15
Welding speed/m/min	0.2–0.4	0.1–0.5
Heat input/J/mm	600–1000	600–1000

The dilution level ($\eta = A_2/(A_1 + A_2)$) of the deposited layers was determined by the fusion of the base steel, indicating the significant differences in the forming characteristics of CMT and PAD deposition layers in Fig. 1. As shown in Fig. 1(c), the penetration crack depth was measured from the fusion line to the lowest end of the crack at a suitable magnification of an optical microscope. In addition, the partial melting zone was defined as the zone near the fusion line where the base steel is not completely melted. First, the width of the partially melted zone was determined on the basis of the melting and microstructural characteristics of the base steel, and then, it was measured using an optical microscope and adjusting the appropriate magnification.

The joints were sliced by wire-cut electric discharge machine (DK7750) to prepare the metallographic and shear specimens. The metallographic specimens were ground to sand paper of grade 2000, then polished, and etched with 8.3 g $FeCl_3 \cdot 6H_2O + 5$ ml $HCl + H_2O$ solution. The microstructures were observed by optical microscopy (Zeiss Axio Vert.A1). The microstructure and elemental distribution were analyzed using an S-3400 scanning electron microscope (SEM) with 20 kV and SE2 detector and Oxford 6650 energy-dispersive spectroscopy (Japan). The phase constitutions of six testing samples were determined using a Bruker D8 advance X-ray diffractometer (XRD) with a scanning speed of $4^\circ/\text{min}$, ranging from 20° to 90° and a voltage of 40 kV and a current of 30 mA with Cu K-alpha radiation. The microhardness test with 12 points per specimen was carried out by Vickers microhardness tester (HXD-1000TM) at a load of 200 g and a dwell time of 10 s. The shearing device and specimen dimensions for measuring shear strength are described in details in Fig. 2. After preparing the deposited layer using CMT and PAD, a shear specimen of 3 mm \times 3 mm \times 15 mm was cut along the cross-section and the shear location was at the interface. The shearing

Fig. 1 Measurement method of dilution rate, wetting angle, and penetration crack of the weld geometry of CMT and PAD, **a** CMT, **b** PAD, and **c** penetration crack

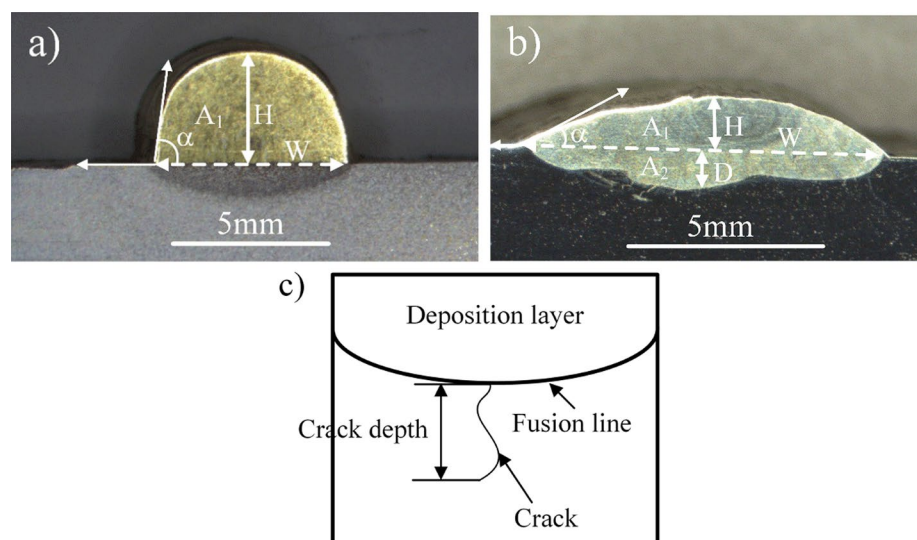
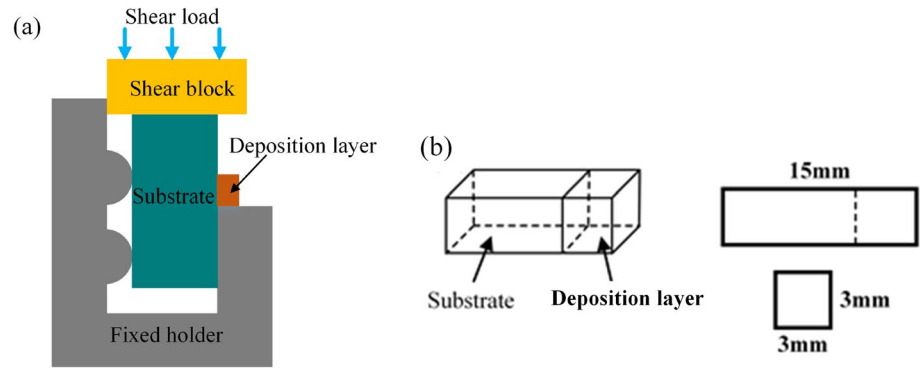


Fig. 2 Schematic diagram of the deposited sample assembly: **a** clamp and **b** specimen size



test was carried out with the electronic universal material testing machine (WE-50, maximum test force 50 kN). The displacement velocity of shearing specimens was 1 mm/min.

3 Results and discussion

3.1 Macrostructures

Figure 3 presents light-optical images of CMT deposited layer in different heat inputs. As illustrated in Fig. 3, the deposited layer exhibited a semicircular profile, and the width of deposited layers (W_D) become larger as heat input increased, and the height of deposited layers (H_D) changed less. From the macroscopic morphology of fusion zone and interface of the deposited sample, no pores and solidification cracking were observed. In addition, the interface of CMT deposited layer presented a straight shape, and the base steel was not melted, which demonstrated diffusion bond properties with less than 900 J/mm of heat input. This is mostly because CMT has a modest heat input, which prevents the molten metal from spreading out completely over the substrate. A robust metallurgical link between the deposited

layer and substrate, however, needed a moderately significant melting of the substrate that ensured some degree of dilution.

Figure 4 illuminates cross-section of PAD deposited samples with different heat inputs. As seen in Fig. 4, the fusion width, penetration depth, and dilution ratio increased with the increased heat input because of the significantly increased arc force during PAD depositing. The result of this present work showed that complete fusion of the deposited layers with the substrate was realized, even at lower heat input. Since the majority of the energy input of PAD was directly used to heat the surface of the base steel, melting zone (A_2) of PAD deposited samples increased more rapidly than that of CMT. As a result, the PAD method has enormous potential for depositing form and repairing bronze components.

Figure 5 shows the contact angle and dilution ratio of CMT and PAD deposited layers in different heat inputs. As illustrated in Fig. 5, the dilution rate of PAD was significantly higher than that of CMT due to the concentrated energy of plasma arc, which had an enhanced effect on the excavation of melt pool and creates a larger penetration depth. When heat input is 900 J/mm, the dilution rate of

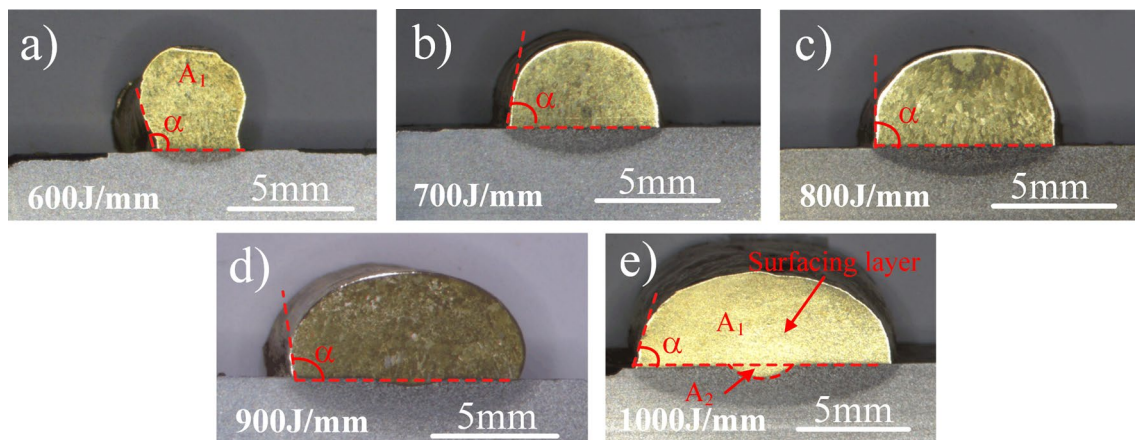


Fig. 3 Optical micrograph of cross-section of CMT single deposition layers, **a** 600 J/mm, **b** 700 J/mm, **c** 800 J/mm, **d** 900 J/mm, **e** 1000 J/mm

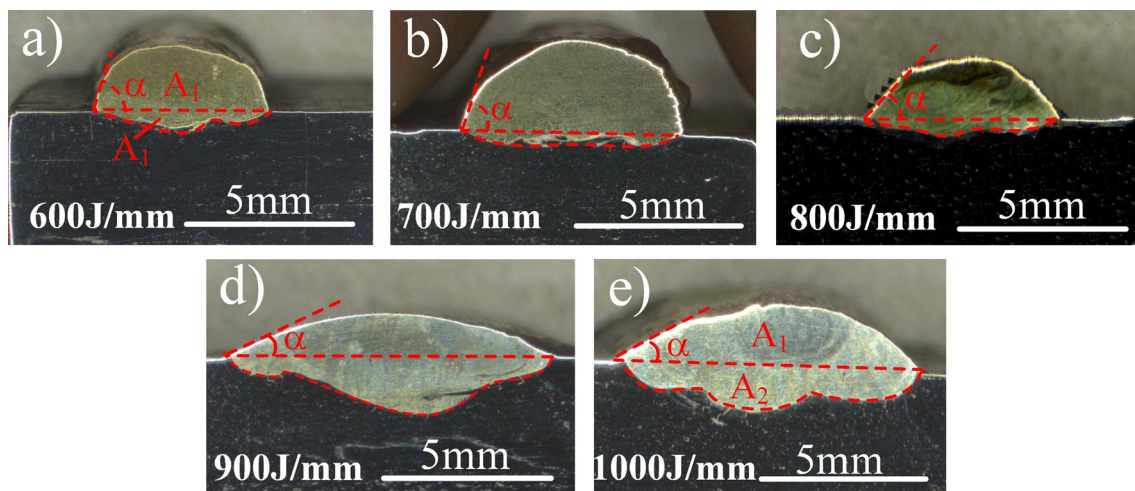


Fig. 4 Optical micrograph of cross-section of PAD single deposition layers, **a** 600 J/mm, **b** 700 J/mm, **c** 800 J/mm, **d** 900 J/mm, **e** 1000 J/mm

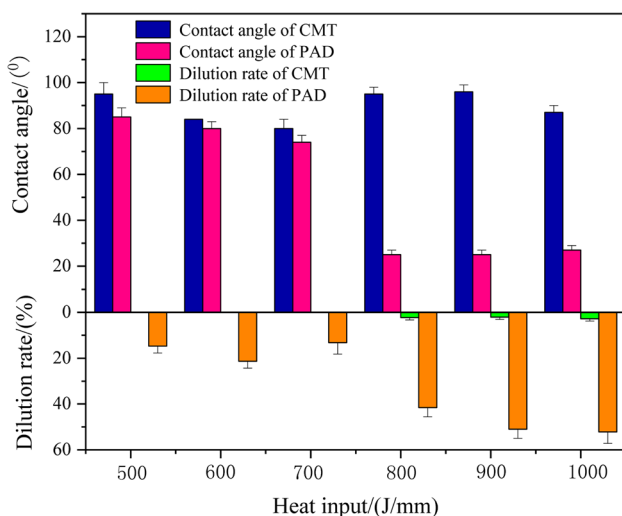


Fig. 5 Contact angle and dilution ratio of CMT and PAD deposited layers in different heat input

PAD reached 50%, and CMT was only 3%. Furthermore, for heat inputs less than 700 J/mm, the contact angle of PAD and CMT deposits differed slightly. With 800 J/mm heat input, the contact angle of CMT deposits had already reached 95°, but that of PAD was only around 25°. During the PAD deposition, the surface of the substrate steel was fully melted, increasing the wetting and spreading of the molten metal.

The molten pool with higher temperature can be established on the steel to promote the wettability of the melt metal as plasma arc used as a heating source. This principle was reported by Zhang et al. [24]. Hence, in the condition of the same deposition rate, the effect of plasma arc heating can improve the wettability of molten metal, and then, a lower

contact angle of deposits can be obtained. Pickin et al. [25] pointed that the contact angle of more than 90° not only resulted in non-uniform bead deposition, but also potential voids could occur between each successive deposited pass. The obtained contact angle of CMT joint was close to 90°. Therefore, under the premise of access to excellent wettability, the welding current can be further improved and the welding efficiency can also be increased.

Figure 6 shows the interface morphology of copper alloy and steel bimetal structure by CMT depositing. The fusion border of intercrystalline penetration of copper alloy into steel was dense and free of discontinuities, as shown in Fig. 6. The colors of aluminum bronze and steel differed noticeably, and the interface demarcation line was visible. As shown in Fig. 6(a), no penetration cracks were found near the interface with low heat input (600 J/mm). The element diffusion on both sides of the interface was weak at low heat input, and the high-temperature residence time and activity of liquid metal were reduced, making it difficult for bronze elements to penetrate along the grain boundaries in the heat-affected zone. As heat input increases, the energy absorbed by the deposit layer increases, and the high-temperature residence time of the substrate increased. The bronze alloys near the deposit layer interface penetrated into the substrate, and small penetration cracks developed around the interface, as shown in Fig. 6(b–d).

Figure 7 shows macroscopic morphology near the interface of PAD deposited layer under different heat inputs. As displayed in Fig. 7a, the dilution rate of PAD deposit layer was low, and a small amount of microcracking appeared near the interface with less than 600 J/mm heat input. When the heat input exceeded 600 J/mm, the dilution rate increased dramatically, and the deposit layer interface showed large variations. In Fig. 7b–d, the grains in the heat-affected zone

Fig. 6 Morphology near the interface of copper alloy and low alloy steel samples for CMT: **a** 600 J/mm, **b** 700 J/mm, **c** 900 J/mm, and **d** 1000 J/mm

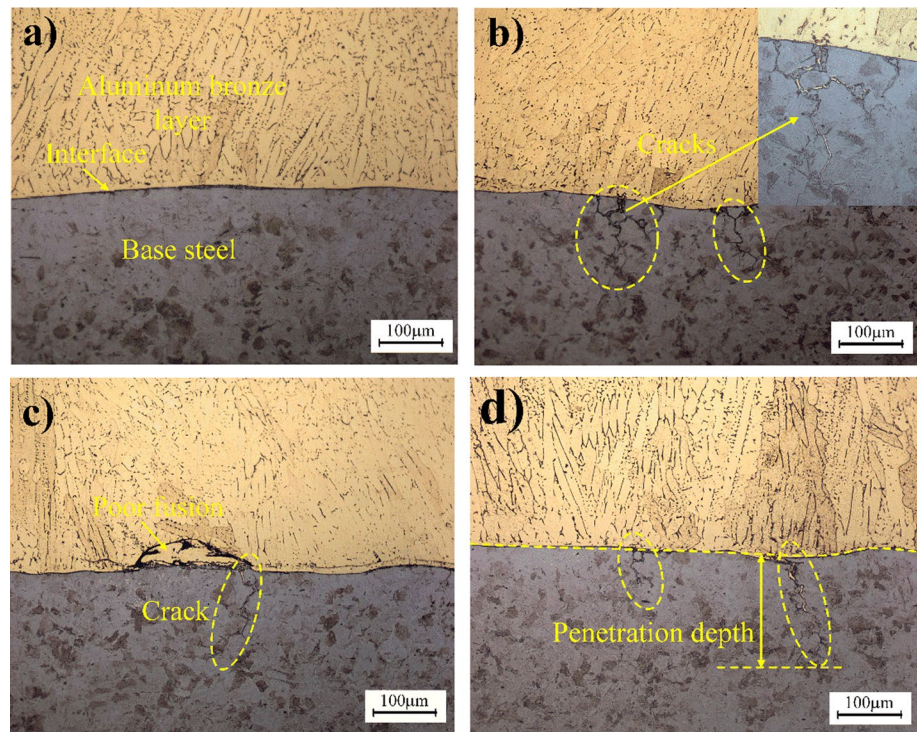
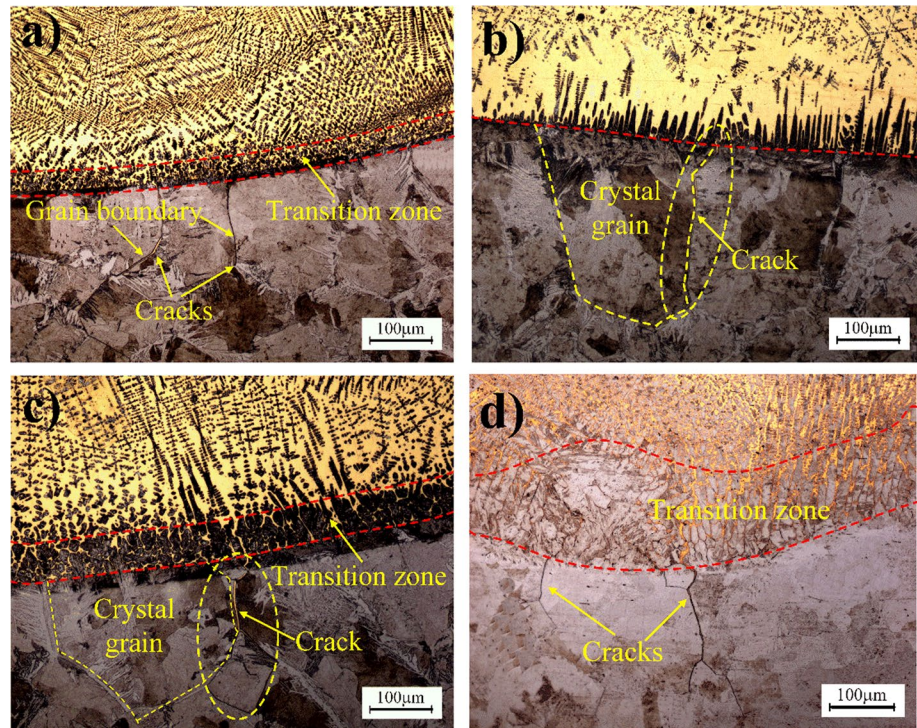


Fig. 7 Morphology near the interface of copper alloy and low alloy steel bimetal structure for PAD. **a** 600 J/mm, **b** 700 J/mm, **c** 900 J/mm, and **d** 1100 J/mm



showed apparent coarsening, and the bronze metal liquid along the grain boundary directly pierced into the internal base steel, resulting in extensive penetration cracks initiating in the solidification crystallization. The high-temperature residence time in the molten pool and the contact time

near the interface between the solid and liquid phases in PAD deposition become longer, and then, diffusion and penetration opportunities increased between the base steel and bronze, resulting in a significant increase in penetration cracks near the interface.

Figure 8 presents the maximum crack length of PAD and CMT deposits at different heat inputs. As the heat input increases, the dilution rate and grain size in the heat-affected zone of both CMT and PAD deposits increased, and the penetration cracking tended to become more severe. In addition, the maximum penetration cracking depth of PAD deposits was substantially higher than that of CMT deposits. The CMT deposition penetration crack depth increased slightly with increasing heat input, while the PAD penetration crack depth did not change much for less than 900 J/mm. In summary, the penetration cracking in wire-arc deposited copper alloy on steel was not entirely determined by the dilution rate, which was closely related to the grain size of the interface zone and elemental diffusion.

3.2 Microstructures

The microstructure morphology and EDS spectra of a CMT bronze deposited layer are shown in Fig. 9. The base steel could not melt with low heat input, as shown in Fig. 9(a), and less iron could only reach the deposited layer by diffusion, with no iron-rich phase created in the deposited layer. As can be seen from the SEM and EDS in Fig. 9(b), the bottom of the deposit layer presented α -Cu columnar crystal, and the middle and upper part was cellular or columnar dendrite, and the precipitated phase presented intermittent distribution along the grain boundary. Microstructure of CMT deposit layer with high heat input was similar to that of low heat input in Fig. 9(c), and the grains had a tendency to coarsen. During the cooling process, β and α -Cu phase at the grain boundaries underwent a co-precipitation transformation to produce γ_1 -phase and α -Cu, and a lamellar black phase located between the

dendrites is formed in Fig. 9(d). Thus, microstructure of CMT deposited layer was a dual-phase structure formed by α -Cu and $\gamma_1 + \alpha$ -Cu eutectic phase.

Figure 10 shows the microstructure of PAD layer under different heat inputs. As heat input increases, the dilution rate of PAD layer increased and more iron entered the deposit layer, which inevitably had a significant effect on the composition distribution and microstructure of deposited layer. When the heat input was 600 J/mm, only a little amount of base steel melted, and the melting depth was not visible, but the breadth of the partial melting zone was about 52 μ m, as shown in Fig. 10a. The lower Fe-rich phase had a plane dendritic, while the upper one had an equiaxed dendrite. In deposited layers, a limited amount of spherical Fe-rich phase is generated. The Fe content and temperature field distribution at different places of the deposited layer were heterogeneous due to the quicker cooling of the melt pool at low heat input. As a result, the composition and shape of the Fe-rich phase differed significantly across the deposited layer.

As shown in Fig. 10d, e, more of the base steel melted with a larger melting depth and a partial melting zone width of 55 μ m when heat input was increased to 700 J/mm. A coarse Fe-rich honeycomb structure was formed in the deposited layer near the interface, while the middle of the deposited layer showed Fe-rich dendritic crystals. The distribution of Fe-rich phase in the deposit layer was not uniform, with obvious bands of Fe-rich phase appearing at the bottom of the deposit layer and less in the upper part. When arc voltage and current (heat input) were high, the electromagnetic stirring effect of arc was enhanced, and meanwhile, under the action of the arc blowing force and molten pool metal flowed, the molten base steel melted to form the iron liquid flowing with the molten pool. Moreover, when the cooling rate of molten pool is fast, the molten iron solidifies in the deposited layer before it is fully diffused in the deposited layer, resulting in uneven distribution of Fe-rich phase.

As seen in Fig. 10(g–l), the dilution rate of the deposited layer increases and more Fe-rich phases are produced as heat input was increased further. The lower grains of the deposited layer transitioned from dendritic to cellular dendritic and cellular crystals, whereas the top grains transitioned from dendritic to cellular or equiaxed. The heat transmitted to the substrate by the arc and the melting wire was the main source of the iron-rich phase during PAD deposition, and the shape and distribution of the iron-rich phase were controlled by both heat input and arc force. When the heat input was large, the melt pool flow and heat and mass transfer time were prolonged, and the Fe-rich phase did not show significant bias aggregation and was more uniformly distributed. Consequently, the Fe-rich phase content increased significantly and become larger in size.

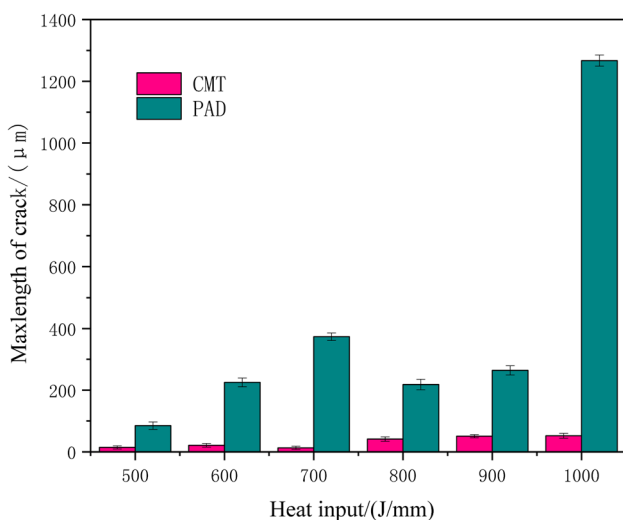
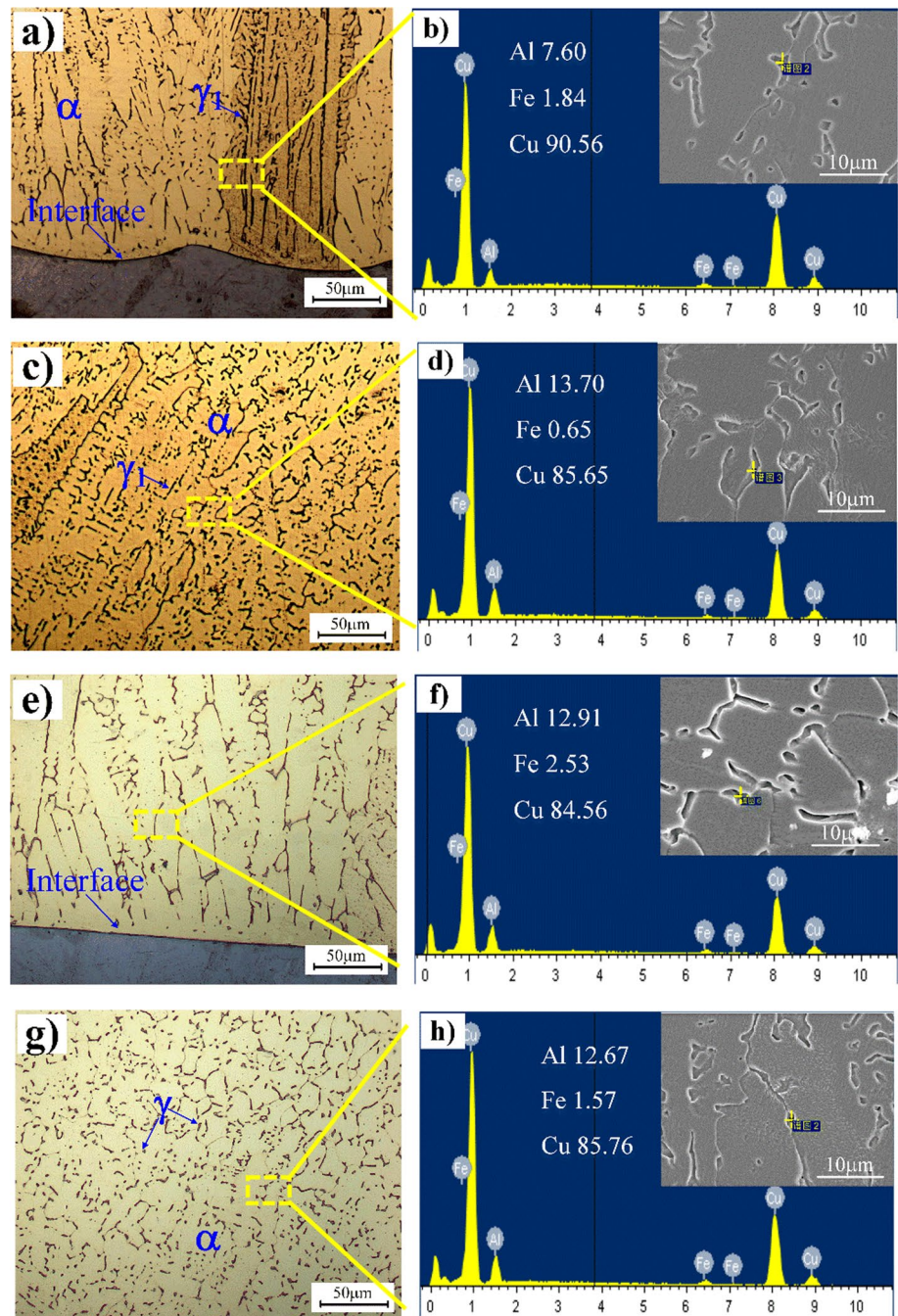


Fig. 8 Maximum penetration crack length of PAD and CMT deposits at different heat inputs

Fig. 9 Optical cross-sectional micrograph and EDS spectrum of deposited layer: **a–d** 600 J/mm, **e–h** 1000 J/mm, **a, e** interface, and **c, g** deposition layer



During deposition, when the Fe content exceeded the maximum solid solution amount of α -Cu, the Fe-rich phase was first precipitated in the form of small particles. With the increase of dilution rate, the Fe content in the deposited layer increased and larger size of Fe-rich phase appeared, forming a Fe-based solid solution dominated by dendritic and cellular crystals. At low heat input, the Fe-rich phase was distributed on the Cu-based solid solution. When the heat input was large, the microstructure of the deposited layer was dominated by coarse and blocky

Fe-rich phases, and a Cu–Al–Fe ternary eutectic phase exists between the Fe-rich phases.

To further determine the phase composition in the deposit layer, energy spectral analysis was performed at different locations in the deposit layer as displayed in Fig. 11. The results of the energy spectrum analysis indicate that these phases are composed of aluminum, iron, and copper. The Fe-dominated solutions are probably Fe-rich fcc solid solutions (γ -Fe) and bcc martensitic structure (α -Fe). The Cu-dominated solutions, on the other hand, are Cu-rich FCC solid

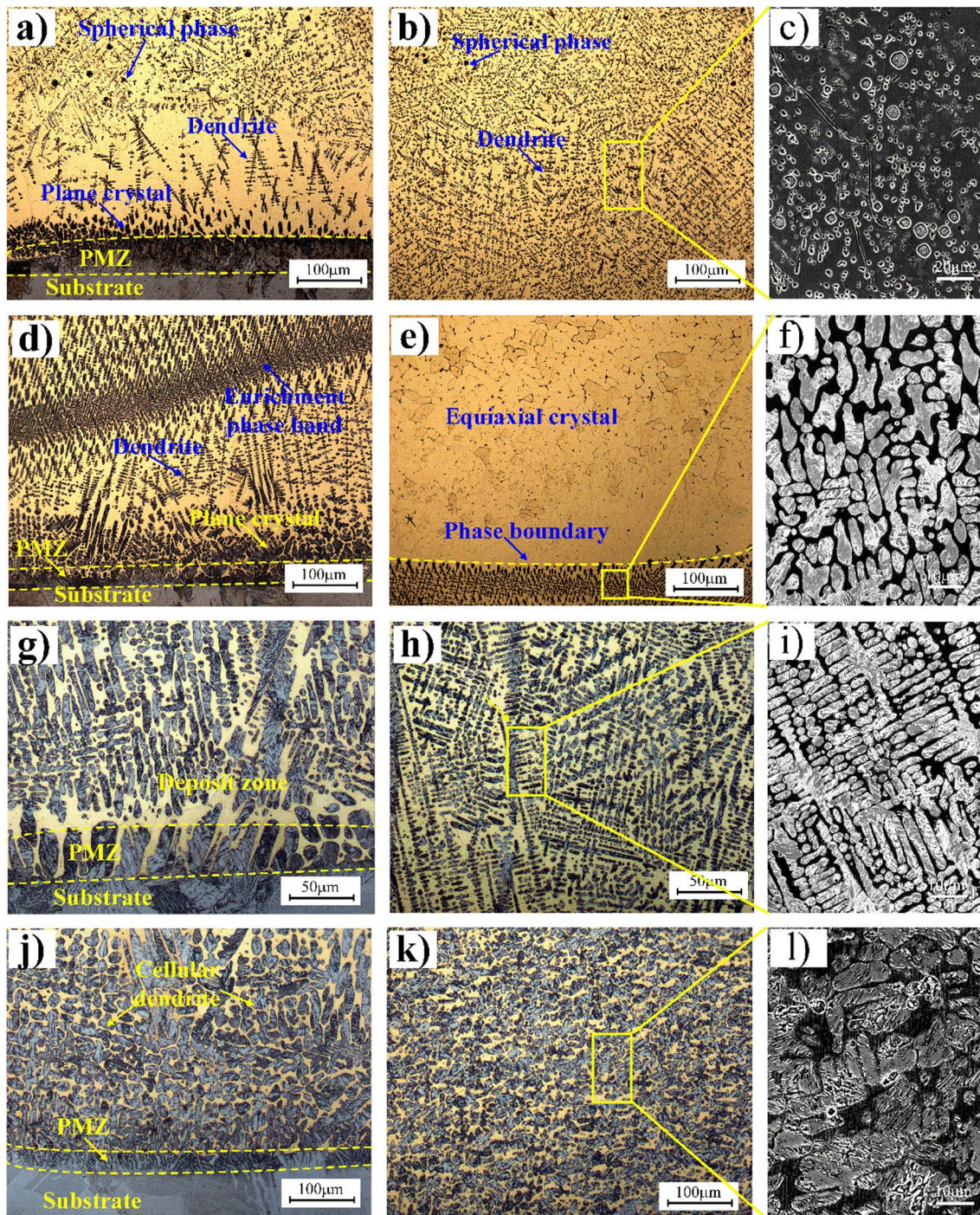


Fig. 10 Microstructure of PAD surfacing layer at the **a, b, c** 600 J/mm, **d, e, f** 700 J/mm, **g, h, i** 900 J/mm, and **g, k, l** 1000 J/mm

solutions (often referred to as α -Cu phases). Figure 11(a) shows energy spectrum near the interface of PAD bronze depositing at low heat input. As presented in Fig. 11a, the microstructure of partially molten zone was ϵ -Cu solid solution, distributed as needles or particles on an acicular martensitic matrix, with a Cu content of about 10%. The black phase near the interface was ϵ -Cu solid solution, which

contained a certain amount of Fe, Al, and other alloying elements, with a Cu content of about 88%. The gray–white columnar crystals appearing near the ϵ -Cu phase were the iron-rich phase, mainly martensite, with a Cu content of about 14%. As demonstrated in Fig. 11(b), a small amount of granular phase with a diameter of 30 μm appeared in the deposited layer, and the energy spectrum analysis indicates

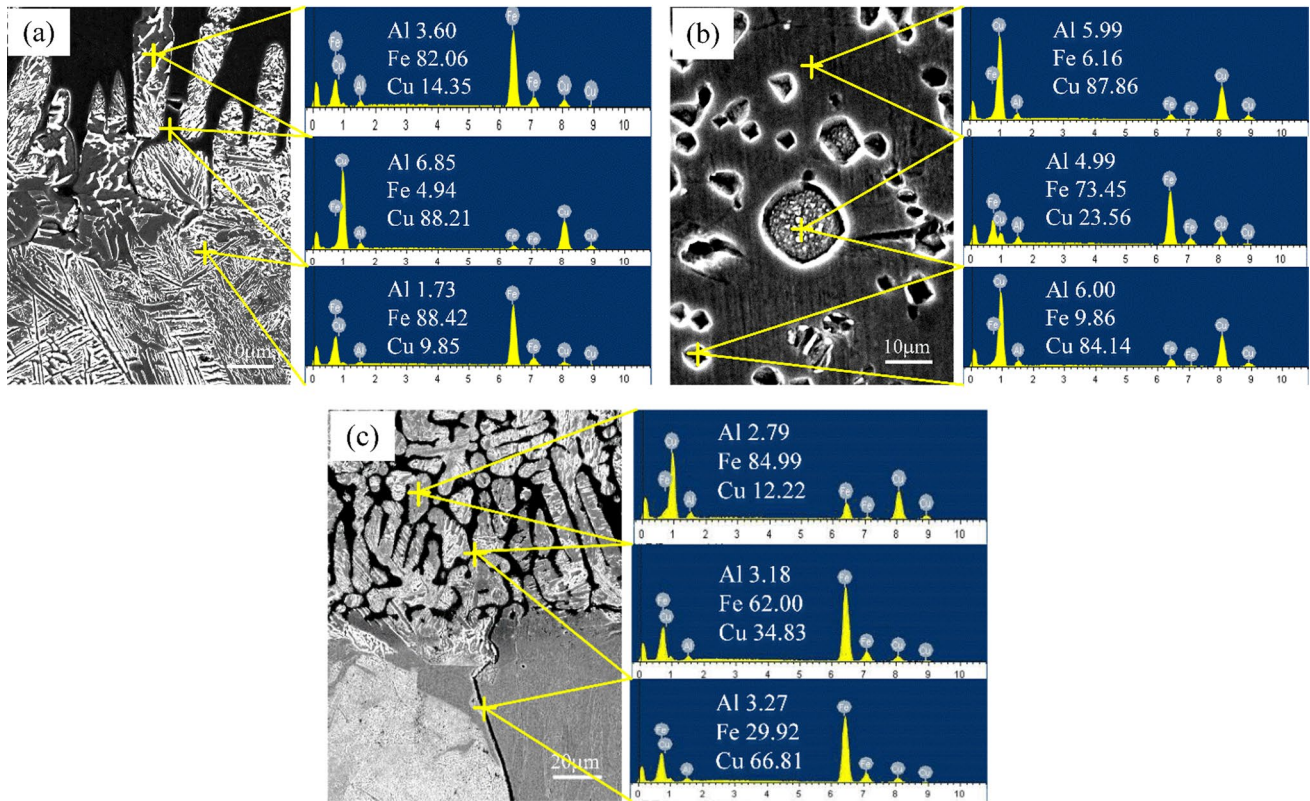


Fig. 11 Energy spectrum near the interface of PAD deposition layers: **a**, **b** 600 J/mm and **c** 1000 J/mm

that it was α -Fe solid solution containing supersaturated Cu, mainly acicular martensite. The energy spectrum analysis near the interface of the bronze deposited layer under high heat input is shown in Fig. 11(c). The Fe-rich phase existed as a Fe-based solid solution and partially undergoes phase change, generating hard and brittle martensite, due to the huge amount of base steel melting into the deposited layer.

To determine the distribution of the composition near the interface of the deposit layer, the interface areas of CMT and PAD deposit layers were analyzed by EDS energy surface scanning, and the test results are revealed in Fig. 12. As illustrated in Fig. 12a, no gradient change of elements appeared along the interface of the CMT deposit layer, and no significant segregation of elements occurred. It should be emphasized that the deposit layer and substrate are bonded using a diffusion method. Figure 12(b) shows the composition distribution near the PAD interface, and a large amount of Fe elements were fused into the deposit layer, and a small amount of Cu diffused into the substrate, and the interface was not obvious, and the concentration of each element at the interface was distributed in a gradient. As a result, a typical metallurgical bond was formed between the deposited layer and the substrate. The deposited layer was dominated by Fe-rich phase and Cu–Al–Fe ternary eutectic, and the distribution of Al elements was relatively uniform.

Figure 13 shows EDS line scan of the deposit layer with different dilution rates. As depicted in Fig. 13(a), the content of Fe, Al, and Cu changed at the interface bond, and the elements were distributed more uniformly in other regions when the dilution rate was low. When more matrix steel melted, the composition transition zone appeared at the interface, and the fluctuation of Fe and Cu elements in the deposited layer was obvious due to the formation of dendritic Fe-rich phase on the copper-based solid solution. The Fe content in the deposited layer exceeded the Cu content, the Fe-rich phase dominated, and a ternary co-crystal was formed between the coarse dendritic crystals when more than 50% dilution rate. Furthermore, the Fe and Cu elements showed gradients throughout the interface, whereas the Al element was totally diffused and equally dispersed.

Figure 14 presents XRD patterns of different areas of CMT and PAD deposits. As displayed in Fig. 14, Cu-rich phases in both CMT and PAD deposit layers were Cu_3Al and Cu_9Al_4 , with Cu mass fraction of about 86% in Cu_3Al and 82% in Cu_9Al_4 , which coincided with the EDS point scan composition. The presence of Fe elements in the depositing layer was in the form of AlFe_3 and AlFe , and the diffraction peaks of Fe compound phases were more significant at the PAD depositing layer and interface.

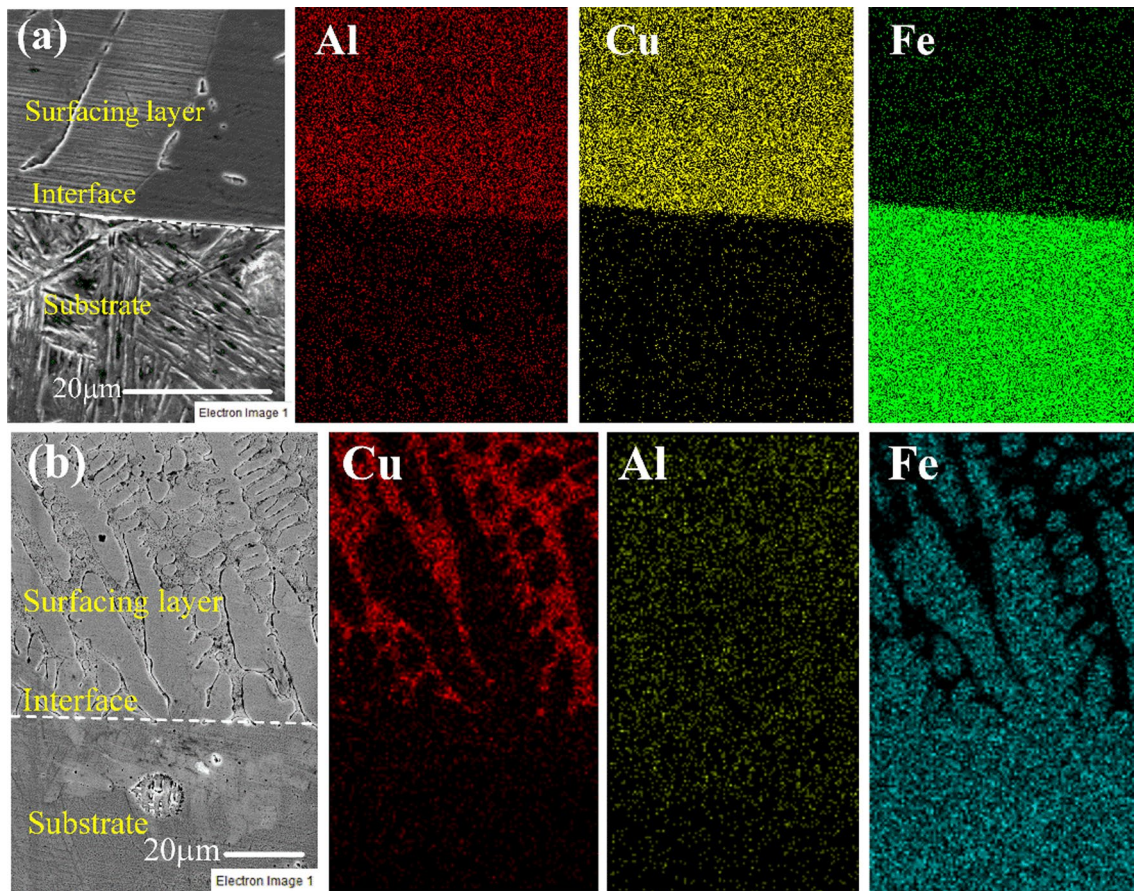


Fig. 12 Elemental distribution near the interface of PAD and CMT layers: **a** CMT, 700 J/mm and **b, c** PAD, 700 J/mm

3.3 Microhardness

Figure 15 shows microhardness distribution of CMT and PAD deposit layers. As seen in Fig. 15, microhardness of CMT deposited layer at high heat input was higher than that at low heat input, and was not significantly different from that of the base steel, which was attributed to the enhanced diffusion of Fe and Cu elements at high heat input, as well as the simultaneous enhancement of heat-affected zone and deposited layer. The microhardness of PAD at low heat input was not much different from that of CMT, but at higher heat input, the base steel melted a lot and the deposit layer transitions from a Cu-based solid solution dominated by low heat input to an Fe-rich phase dominated by high heat input, resulting in a significant increase in deposit hardness from 170 HV at low heat input to 350 HV at high heat input. A little quantity of Fe reached the deposit layer, producing a minor amount of Fe-rich phase that did not significantly add to the hardness of the bronze deposit layer. More Fe-rich phases were generated on Cu-based alloys as a

result of a substantial number of Fe elements entering the deposit layer. The effect of higher dilution and more Fe-rich phase of PAD on microhardness were considerable.

During the wire-arc deposition process, the heat-affected zone near the fusion line is sharply heated and rapidly cooled, and the temperature instantaneously rises above the Ac3 line, and the ferrite and pearlite in the substrate undergoes recrystallization and transforms into equiaxed austenite and a small amount of martensite, so the hardness of the heat-affected zone is slightly increased compared with that of the substrate [26]. In addition, the width of the heat-affected zone of CMT under low heat input is narrow, the residence time at high temperature is short, and the diffusion of alloying elements of the aluminum-bronze deposited layer into the heat-affected zone is weakened, and its hardness is not much different from that of the base steel. Although the heat inputs of the CMT and PAD used in this paper are consistent, the differences in their energy conversion efficiencies and fusion behaviors result in hardnesses that show significant differences.

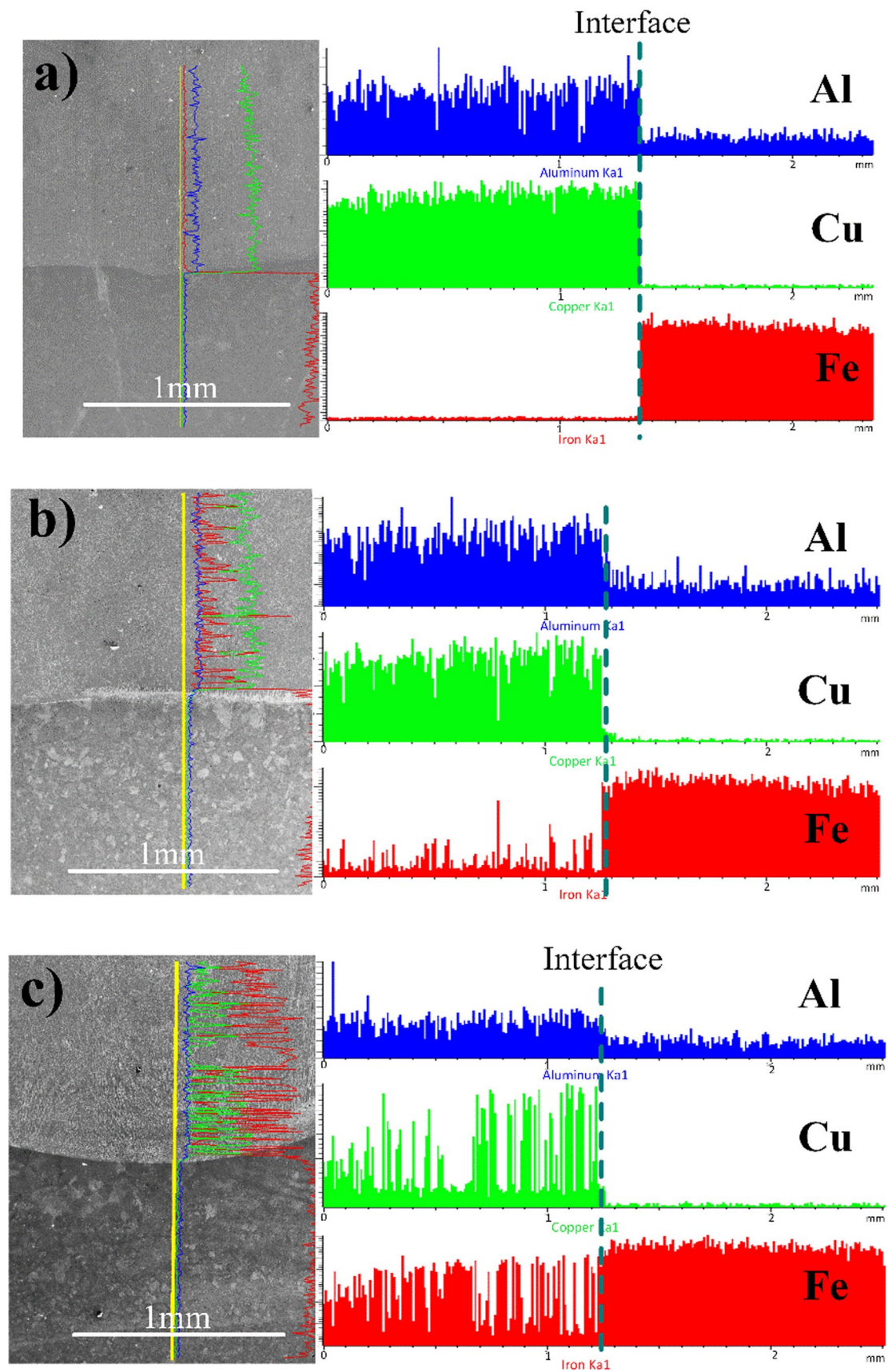


Fig. 13 EDS line scanning of the deposit layer in different dilution rates: **a** 0.2%, **b** 19%, and **c** 53%

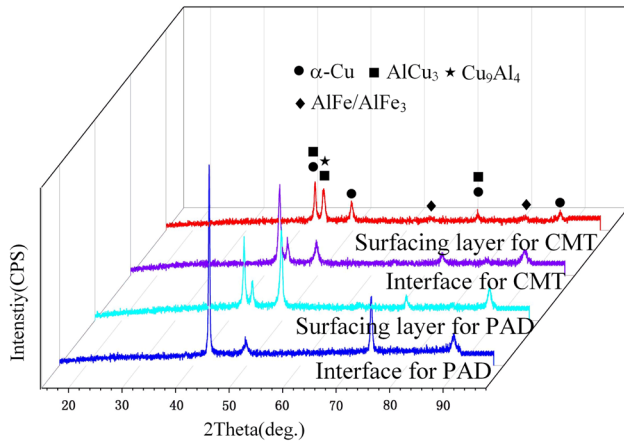


Fig. 14 XRD patterns of different regions of CMT and PAD surfacing samples

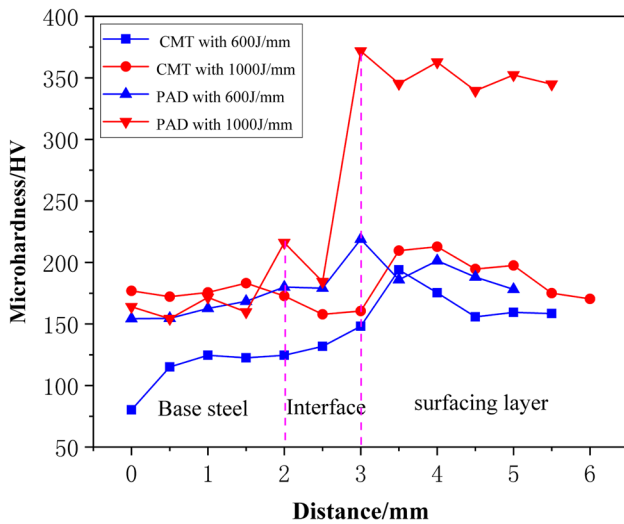


Fig. 15 Microhardness distribution of CMT and PAD deposit layers in different heat inputs

3.4 Shear strength

The bonding contact between incompatible material components is frequently the weak point. An interfacial shear test was performed to characterize the binding strength at the interface between the deposited layer and the substrate. Figure 16 shows the displacement–stress curves from the shear test. As presented in Fig. 16, the shear strength of CMT deposited layer with low heat input was not significantly different from that of the high heat input. The shear strength of PAD deposited layer with low heat input was higher than that of the high heat input, but both were significantly higher than that of the CMT. The average shear strength of the CMT specimens was 135 MPa, while the average shear strength of the PAD specimens was 350 MPa.

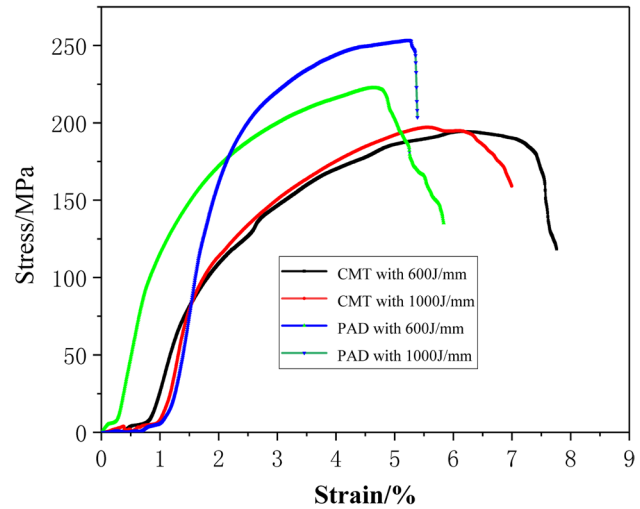


Fig. 16 The displacement–stress curve of CMT and PAD deposited layers in different heat input

The interfaces of PAD deposited layers with identical diffusion connections demonstrated better shear strengths, higher dilution rates, and sufficient metallurgical reactions.

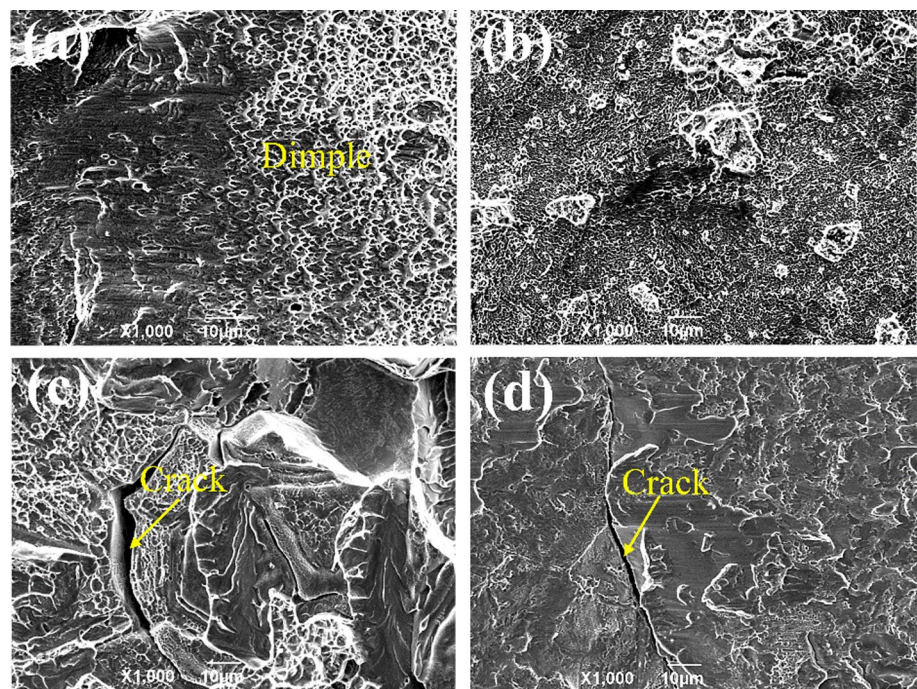
Figure 17 shows fracture morphology of the shear specimens with CMT and PAD deposited layers. As illustrated in Fig. 17, the shear specimens fractured at the interface area, and the fracture of CMT specimens was dominated by dimples, which was typical of ductile fracture. The shear fracture of a PAD deposited layer under low heat input was a heterogeneous ductile fracture with coexistence of cleavage steps and dimples, as well as penetration fractures. Under high heat input, the PAD fractures were apparent brittle fractures dominated by slip lines and cleavage stages, with obvious penetration cracks. More base steel melted and infiltrated the deposited layer as heat input increased, resulting in a non-uniform distribution of components and microstructure in the deposited layer, but strong metallurgical bonding at the interface. Also, a considerable number of penetration cracks formed along the interface of the PAD deposited specimens, which was detrimental to the interface’s bonding strength.

4 Conclusions

In this study, an aluminum-bronze alloy coating was fabricated on the mild steel substrate by PAD and CMT process. The microstructure of interface layer and the mechanical properties of fabricated component were investigated. Conclusions from the study are drawn as follows:

- (1) CMT deposition specimens exhibited less dilution and were less influenced by heat input. The dilution rate of PAD deposited specimens increased with increasing

Fig. 17 Fracture surface morphology of CMT and PAD surfacing layer: **a, b** CMT, **c, d** PAD, **a, c** 600 J/mm, and **a, b** 1000 J/mm



heat input, indicating excellent metallurgical bonding to the substrate.

- (2) The penetration crack size of CMT deposited specimens significantly smaller than that of PAD. The depth and number of penetration cracks increased with increasing dilution.
- (3) The distribution of Fe in the deposited layer with increasing dilution rate presented a clear layering phenomenon, and the microstructure of the deposited layer changed from α -Cu + spherical and dendritic Fe-rich phase to massive Fe-rich phase + ϵ -Cu as dilution increased.
- (4) Microhardness of CMT and PAD layers was greatly influenced by the amount and morphology of Fe-rich phase. The interfacial bond strength of PAD was significantly higher than that of CMT.

Acknowledgements This work was supported by the Natural Science Fund of Anhui Province Education Office No. 2022AH0S0322.

Author contributions YW: conceptualization, methodology, and writing—review and editing. XW: data curation, and writing—original draft. JZ: investigation and resources. ZL: formal analysis. CH: validation. WM: project administration. Jh: supervision.

Data availability The authors confirm that the data supporting the findings of this study are available within the article.

Declarations

Conflict of interest The authors declare that they have no known competing financial interests or personal relationships that could have appeared to influence the work reported in this paper.

References

1. F. Yang, H. Kang, E. Guo, R. Li, Z. Chen, Y. Zeng, T. Wang, The role of nickel in mechanical performance and corrosion behaviour of nickel-aluminum bronze in 3.5 wt.% NaCl solution. *Corros. Sci.* **139**, 333–345 (2018)
2. B.P. Pisarek, B. Kowalski, H. Atapek, S. Polat, T. Tüfekçi, Microstructural and tribological characterization of aluminum bronzes with additions of Si and Cr. *Arch. Foundry Eng.* **18**, 93–98 (2018)
3. C. Chen, Q.M. Xu, K. Sun, J.Y. Zhao, J. Zhou, F. Xue, Tin-bronze cladding on thin steel sheet by cold metal transfer arc deposition. *Mater. Sci. Technol.* **35**, 1526–1529 (2018)
4. J. Chen, Y.Q. Yang, C.H. Song, M.K. Zhang, S.B. Wu, D. Wang, Interfacial microstructure and mechanical properties of 316L/CuSn10 multi-material bimetallic structure fabricated by selective laser melting. *Mater. Sci. Eng. A* **752**, 75–85 (2019)
5. Q.Y. Hou, T.T. Ding, Z.Y. Huang, P. Wang, L.M. Luo, Y.C. Wu, Microstructure and properties of mixed Cu-Sn and Fe-based alloys with molybdenum addition processed by plasma transferred arc. *Surf. Coat. Technol.* **283**, 184–193 (2015)
6. G. Zhang, W.Y. Li, Y. Gao, H.L. Li, C. Coddet, Investigation of the microstructure and tribological behavior of cold-sprayed tin-bronze-based composite coatings. *Appl. Surf. Sci.* **255**, 3822–3828 (2009)

7. Z. Cheng, J.H. Huang, Z. Ye, Y. Chen, J. Yang, S.H. Chen, Microstructures and mechanical properties of copper-stainless steel butt-welded joints by MIG-TIG double-sided arc welding. *J. Mater. Process. Tech.* **265**, 87–98 (2019)
8. G. Mou, X.M. Hua, M. Wang, F. Li, Effects of Ni addition on removing Fe-Ti intermetallic compounds in cold metal transfer arc-brazed TC4/304L dissimilar joints. *J. Manuf. Process.* **38**, 104–112 (2019)
9. J.L. Xu, B. Yang, W. Gao, Z.P. Wang, D.W. Long, C.Y. Ju, T. Yu, Microstructure and performance of laser cladding on surface of aluminum bronze. *J. Aeronaut. Mater.* **29**, 63–67 (2009)
10. A. Sadeghi, A. Moloodi, M. Golestanipour, M.M. Shahri, An investigation of abrasive wear and corrosion behavior of surface repair of gray cast iron by SMAW. *J. Mater. Res. Technol.* **6**, 90–95 (2017)
11. M.H. Sohi, M. Ebrahimi, H.M. Ghasemi, A. Shahripour, Microstructural study of surface melted and chromium surface alloyed ductile iron. *Appl. Surf. Sci.* **258**, 7348–7353 (2012)
12. M. Pascual, J. Cembrero, F. Salas, M.P. Martínez, Analysis of the weldability of ductile iron [J]. *Mater. Lett.* **62**, 1359–1362 (2008)
13. K.Y. Chen, X.F. Yang, W.Y. Li, G.F. Xia, S.R. Wang, K. Wang, Study on the wear and corrosion resistance of Fe–Mo coatings on 65Mn steel ploughshares by laser cladding. *Appl. Phys. A-Mater.* **128**, 795 (2022)
14. N. Jordan, R. Schröder, H. Harig, R. Kienzler, Influences of the spray deposition process on the properties of copper and copper alloys. *Mater. Sci. Eng. A* **326**, 51–62 (2002)
15. Y.H. Zhou, X. Lin, N. Kang, W.D. Huang, J. Wang, Z.N. Wang, Influence of Travel speed on microstructure and mechanical properties of wire + arc additively manufactured 2219 aluminum alloy. *J. Mater. Sci. Technol.* **37**, 143–153 (2020)
16. L.B. Sun, F.C. Jiang, R.S. Huang, D. Yuan, Y. Su, C.H. Guo, J.D. Wang, Investigation on the process window with liner energy density for single-layer parts fabricated by wire and arc additive manufacturing. *J. Manuf. Process.* **56**, 898–907 (2020)
17. A.U. Khan, Y.K. Madhukar, An economic design and development of the wire arc additive manufacturing setup. *Procedia CIRP.* **91**, 182–187 (2020)
18. S. Prasad, S. Pal, P.S. Robi, Analysis of weld characteristics of micro plasma arc welded thin stainless steel 306L sheet. *J. Manuf. Process.* **57**, 957–977 (2020)
19. Y.X. Zhou, J. Zhang, Z.G. Xing, H.D. Wang, Z.L. Lv, Microstructure and properties of NiCrBSi coating by plasma cladding on gray cast iron[J]. *Surf. Coat. Technol.* **361**, 270–279 (2018)
20. L.J. Zhu, Y.H. Liu, Z.W. Li, L. Zhou, Y.J. Li, A.H. Xiong, Microstructure and properties of Cu-Ti-Ni composite coatings on gray cast iron fabricated by laser cladding [J]. *Opt. Laser Technol.* **122**, 105879–105879 (2020)
21. F.M. Ghaini, M. Ebrahimi, S. Gholizade, Characteristics of cracks in heat affected zone of ductile cast iron in powder welding process [J]. *Eng. Fail. Anal.* **18**, 47–51 (2011)
22. Z.K. Weng, A.H. Wang, Y.Y. Wang, D.H. Xiong, H.Q. Tang, Diode laser cladding of Fe-based alloy on ductile cast iron and related interfacial behavior[J]. *Surf. Coat. Technol.* **286**, 64–71 (2016)
23. A. Gulzar, J.I. Akhter, M. Ahmad, G. Ali, M. Mahmood, M. Ajmal, Microstructure evolution during surface alloying of ductile iron and austempered ductile iron by electron beam melting[J]. *Appl. Surf. Sci.* **255**, 8527–8532 (2009)
24. X.C. Zhang, T. Pan, Y.T. Chen, L. Li, Y.L. Zhang, F. Lou, Additive manufacturing of copper-stainless steel hybrid components using laser-aided directed energy deposition[J]. *J. Mater. Sci. Technol.* **80**, 100–116 (2020)
25. C.G. Pickin, S.W. Williams, M. Lunt, Characterization of the cold metal transfer (CMT) process and its application for low dilution cladding. *J. Mater. Process. Technol.* **211**, 496–502 (2011)
26. F.W.C. Fariasa, J.C.P. Filhoa, D.A.S. Júniorb, R.N. Mouraa, M.C.G. Riosa, Microstructural characterization of Ni-based superalloy 625 clad welded on a 9% Ni steel pipe by plasma powder transferred arc. *Surf. Coat. Technol.* **374**, 1024–1037 (2019)

Publisher's Note Springer Nature remains neutral with regard to jurisdictional claims in published maps and institutional affiliations.

Springer Nature or its licensor (e.g. a society or other partner) holds exclusive rights to this article under a publishing agreement with the author(s) or other rightsholder(s); author self-archiving of the accepted manuscript version of this article is solely governed by the terms of such publishing agreement and applicable law.

Authors and Affiliations

Yanming Wu^{1,3} · Xinghua Wang¹ · Jintian Zhang¹ · Zhi Li¹ · Chenghui Hu¹ · Wei Meng⁴ · Jiguo Shan^{2,3}

✉ Jiguo Shan
shanjg@tsinghua.edu.cn

¹ Luoyang Ship Material Institute, Luoyang 437023, China

² Department of Mechanical Engineering, Tsinghua University, Beijing 100084, China

³ Key Laboratory for Advanced Materials Processing Technology, Ministry of Education, Tsinghua University, Beijing 100084, China

⁴ School of Materials Science and Engineering, Anhui University of Technology, Maanshan 243032, China